9-24-2018

Microstructure and coercivity in alnico 9

Lin Zhou
Ames Laboratory, linzhou@ameslab.gov

Emma White
Ames Laboratory, ewhite@ameslab.gov

Liqin Ke
Ames Laboratory, liqinke@ameslab.gov

David A. Cullen
Oak Ridge National Laboratory

Ping Lu
Sandia National Laboratories

See next page for additional authors

Microstructure and coercivity in alnico 9

Abstract
Magnetic property enhancement of alnico, a rare-earth free permanent magnet, is highly dependent on both the initial microstructure and the evolution of the spinodal decomposition (SD) inside each grain during the heat treatment process. The size, shape and distribution of the magnetic FeCo-rich (α1) phase embedded in continuous non-magnetic AlNi-rich (α2) phase as well as a minor Cu-enriched phase residing in between are shown to be crucial in controlling coercivity. Phase and magnetic domain morphology in a commercial alnico 9 alloy was studied using a combination of structural characterization techniques, including scanning electron microscopy, electron backscatter diffraction, aberration-corrected scanning transmission electron microscopy and Lorentz microscopy. Our results showed that casting created structural nonuniformity and defects, such as porosity, TiS2 precipitates and grain misorientation, are heterogeneously distributed, with the center section having the best crystallographic orientation and minimal defects. The optimal spinodal is a "mosaic structure", composed of rod-shape α1 phase with {1 1 0} or {1 0 0} planar faceting and diameter of ~30–45 nm. There is also a Cu-enriched phase residing at the corners of two 〈1 1 0〉 facets of the α1 phase. It was observed that grain boundary phase reverse magnetization direction at lower external magnetic field compared to the SD region inside the grain. Improving grain orientation uniformity, reducing detrimental grain boundary phase volume fraction, and the branching of the α1 rods, as well as their diameter, are promising routes to improve energy product of alnico.

Keywords
Permanent magnets, Microstructure, Spinodal decomposition, Atom-probe tomography, TEM, STEM HAADF, Lorentz microscopy

Disciplines
Materials Science and Engineering

Authors
Lin Zhou, Emma White, Liqin Ke, David A. Cullen, Ping Lu, S. Constantinides, R. W. McCallum, Iver E. Anderson, and Matthew J. Kramer

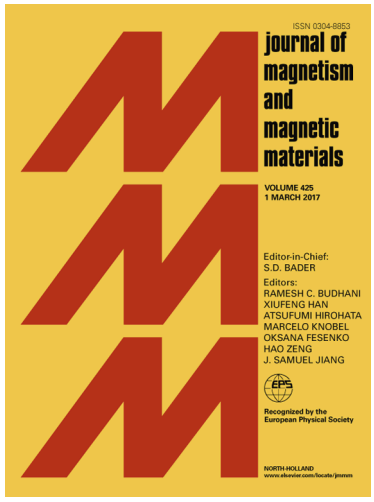

Microstructure and Coercivity in Alnico 9

Lin Zhou, Emma White, Liqin Ke, David A. Cullen, Ping Lu, S. Constantinides, R.W. McCallum, I.E. Anderson, M.J. Kramer

PII: S0304-8853(18)30377-9
DOI: https://doi.org/10.1016/j.jmmm.2018.09.085
Reference: MAGMA 64367

To appear in: *Journal of Magnetism and Magnetic Materials*

Received Date: 9 February 2018
Revised Date: 16 August 2018
Accepted Date: 22 September 2018

Please cite this article as: L. Zhou, E. White, L. Ke, D.A. Cullen, P. Lu, S. Constantinides, R.W. McCallum, I.E. Anderson, M.J. Kramer, Microstructure and Coercivity in Alnico 9, *Journal of Magnetism and Magnetic Materials* (2018), doi: https://doi.org/10.1016/j.jmmm.2018.09.085

Microstructure and Coercivity in Alnico 9

Lin Zhou, [1,*] Emma White,[1] Liqin Ke,[1] David A. Cullen,[2] Ping Lu,[3] S. Constantinides,[4] R.W. McCallum,[1] I. E. Anderson, [1] and M. J. Kramer [1]

[1] Ames Lab, Ames, IA 50014

[2] Materials Science and Technology Division, Oak Ridge National Laboratory, Oak Ridge, TN 37831

[3] Sandia National Laboratories, PO Box 5800, MS 1411, Albuquerque, NM 87185

[4] Arnold Magnetic Technologies Corporation, Rochester, NY 14625

Abstract:

Magnetic property enhancement of alnico, a rare-earth free permanent magnet, is highly dependent on both the initial microstructure and the evolution of the spinodal decomposition (SD) inside each grain during the heat treatment process. The size, shape and distribution of the magnetic FeCo-rich (α_1) phase embedded in continuous non-magnetic AlNi-rich (α_2) phase as well as a minor Cu-enriched phase residing in between are shown to be crucial in controlling coercivity. Phase and magnetic domain morphology in a commercial alnico 9 alloy was studied using a combination of structural characterization techniques, including scanning electron microscopy, electron backscatter diffraction, aberration-corrected scanning transmission electron microscopy and Lorentz microscopy. Our results showed that casting created structural nonuniformity and defects, such as porosity, TiS_2 precipitates and grain misorientation, are heterogeneously distributed, with the center section having the best crystallographic orientation and minimal defects. The optimal spinodal is a "mosaic structure", composed of rod-shape α_1 phase with {110} or {100} planar faceting and diameter of ~30-45nm. There is also a Cu-enriched phase residing at the corners of two <110> facets of the α_1 phase. It was observed that grain boundary phase reverse magnetization direction at lower external magnetic field compared to the SD region inside the grain. Improving grain orientation uniformity, reducing detrimental grain boundary phase volume fraction, and the branching of the α_1 rods, as well as their diameter, are promising routes to improve energy product of alnico.

Keywords: *Permanent Magnets, Microstructure, Spinodal decomposition, Atom-probe tomography, TEM, STEM HAADF, Lorentz microscopy*.

1. Introduction

Permanent magnets (PM) play an important role in motors and generators for hybrid electric vehicles, wind turbines and many other energy-efficient appliances.[1, 2] The efficiency of the energy conversion depends on the magnetic properties of the PM which is mainly characterized by remanence (B_r), intrinsic coercivity (H_{ci}), and maximum energy product ($(BH)_{max}$) [3]. Among the PM materials, neodymium-based alloys provide the highest energy products. However, in order to maintain its high-temperature performance, large amounts of dysprosium (Dy), a key rare-earth element, is added, which causes concern due its cost and supply criticality [1, 4-6]. As a result, searching for a PM material with less or no RE elements has gained worldwide attention. Interest in alnico, a PM alloy system composed mostly of Fe, Al, Co, Ni and Ti, has rekindled due to its good high temperature performance and worldwide abundant supply of the constituent elements. Alnico's upper working temperature is 538°C with a very low reversible change in magnetization of < 0.02%/°C, superior to the rare earth-based permanent magnets [1, 3, 4, 7]. Theoretical research on alnico also indicates that the coercivity may be improved up to ~4000Oe, which is twice that of commercially available alnico alloys [8, 9]. Achieving this level of coercivity will require smaller diameter (< 20 nm) of the α_1 rods and better isolation within the α_2 matrix. Since the major source of coercivity arises from shape anisotropy, the size, shape and distribution of the α_1 rods must be optimized. The volume fraction of the α_1 rods is dependent on the alloy composition while the size and shape of the rods are highly controlled by thermal magnetic processing and their relative alignment to the crystallographic [001] direction of the grain[10].

Using advanced characterization and simulation tools [11-19], in particular aberration-corrected scanning transmission electron microscopy (STEM) and *in-situ* Lorentz microscopy,

we describe the crucial microstructure and magnetization features of a commercial alnico 9 that give rise to the highest energy product of ~10.5MGOe in the alnico family. Armed with this information, key processing and chemical modifications are proposed for further improving the energy product of alnico [20] .

2. Experimental procedure

The alnico 9 alloy was supplied by Arnold Magnetic Technologies Corp with a composition of 35.5Fe-35.4Co-13.1Ni-7Al-5.0Ti-3.2Cu (wt%). It was a directionally solidified alloy with most grains aligned along the [001] direction and was produced by casting into a heated mold with a chilled bottom plate. The cast alloys were heat-treated at about 1250 ºC to fully solutionize the alloy then air-cooled to about 800 ºC, followed by a magnetic field annealing process at ~800ºC with an external magnetic field along the grain aligned/casting direction. Finally, the alloy underwent an extended 'draw' cycle with slow cooling and a temperature hold at approximately 640 ºC.

Transmission electron microscopy (TEM) and scanning TEM (STEM) analysis were performed on both transverse (observation along the magnetic field direction during annealing) and longitudinal (observation perpendicular to the magnetic field direction during annealing) orientations. TEM samples were prepared by mechanical polishing followed by short time, low-voltage Ar ion-milling with a liquid-nitrogen cold stage. An FEI Titan G2 80-200 STEM with Cs probe corrector and ChemiSTEM^{TM} technology, an FEI Tecnai F20 (200 kV, FEG) with Lorentz lens and a Nion UltraSTEM U100 were used for microstructural characterization. STEM was performed mostly in high-angle annular dark-field (HAADF) imaging mode to clearly differentiate phase morphologies and collect elemental information from corresponding spectrum images obtained by energy dispersive X-ray spectroscopy (EDS). Scanning electron microscopy

(SEM) analysis was performed using an FEI quanta FEG 250 instrument. EBSD was performed using an Amray 1845 field emission SEM.

3. Results and discussion

3.1 Microstructure overview

SEM analysis of polished transverse cross-sectional microstructures of the alnico 9 from the cylinders taken from the top, middle and bottom of the casting showed large variation in the grain size and porosity throughout the height of the casting (Fig. 1 (a-c)). The top of the casting showed significant porosity in the sample as demonstrated by the larger dark, rounded features in Figure 1(a). The grain size of the bottom of the chill cast alnico 9 was much finer, ~100μm, compared to ~300μm for the middle and ~400μm for the top of the casting. All three regions had TiS_2 precipitates throughout the cast microstructure, as shown by the small dark grey faceted phases in Figures 1 (a-c). EBSD along the transverse direction of the middle of the alnico 9 revealed that the alloy had a high degree of grain alignment of the <001> along the casting direction (Fig. 1 d and e). Some misoriented grains were also observed, especially near the edge of the cast block. The magnetization data also shows a significant difference between the middle compared to the ends the casting in terms of squarness (Table 1). The best squareness and highest energy product correlating with the best texture observed in the middle of the casting. The top and bottom appears to show slightly higher coercivity, however this range is within the magnitude of the measurement uncertainity of the hysteresisgraph instrument of ±20Oe. Figure 1 (f), a higher magnification SEM image of the bottom of the casting, showed formation of a secondary FeCo-rich phase (brighter contrast) present along the grain boundaries and extending into the grains. The variation in grain sizes from bottom to top are consistent with the initial

random nucleation and higher cooling rate at the bottom of the casting while the higher degree of porosity and 2nd phase due to solute segregation and slower growth near the top.

3.2 Morphology and structure of spinodal phases

HAADF-STEM imaging and EDS mapping were used to quantify the crystallography its chemistry, size and distribution of the spinodal phases. Observing the optimal spinodal along the <001> reveals a nanometer-scale 'mosaic' structure with 'tiles' of α_1 phase ~35-50 nm across(Fig. 2(a)). The size and shape of the "tiles" is not uniform. The "tiles" are linked with ~5nm diameter bright bridges. STEM-EDS elemental mapping (Fig. 2(c)) indicates the bright "tiles" are the FeCo-rich (α_1 phase), which tend to be faceted on their {110} planes and less commonly on {100} planes. Most of the links between "tiles" are actually a Cu-enriched phase, which tends to locate at the corner of two {110} α_1 phase facets. The darker region (α_2 phase) is composed mainly of Al, Ni, Ti and Co. The Ti map covers a smaller area of the α_2 phase when compared to the Al and Ni map. This is due to the deficiency of Ti at the α_1/α_2 interface region. When the α_1 phase is faceted on {100} planes, Ni-rich clusters between two adjacent α_1 rods, as indicated by the black arrow (Fig. 2(c)), are sometimes observed. A color composite EDS image (Fig. 2(c)) clearly shows a Ni-rich region (green shell) at the α_1/α_2 interface. High-resolution HAADF-STEM image (Fig 2 (b)) taken along the [100] zone axis shows coherent α_1/α_2 interface with the epitaxial relationship of [100] $_{\alpha 1}$//[100] $_{\alpha 2}$. Alternating contrast of (100) planes within the α_2 phase also implies chemical ordering. Previous studies using atomic scale EDS mapping found that the α_2 phase was $L2_1$ ordered with site occupancy of $(Ni_{0.48}Co_{0.52})_2(Fe_{0.20}Ti_{0.80})Al$, while the α_1 phase was B2 ordered with site occupancy of $(Fe_{0.76}Co_{0.24})(Fe_{0.40}Co_{0.60})$.[21]

Observation of alnico 9 along the longitudinal direction (Fig. 3(a)) showed that the α_1 precipitates were very long (>400nm). A STEM-EDS color composite of the spectrum images

(Fig. 3 (b)) for Al (green), Fe (magenta) and Cu (orange) shows that the α_1 rods generally had tapered ends with an aspect ratio >10. Branching is commonly observed in the α_1 rods (as indicated by white arrows in Fig. 3 (b)), which, along with the tapered ends, may be a reason for the non-uniform size distribution of α_1 rods observed in the transverse image. The Cu-enriched phase also has a rod-like shape, but its length is much shorter (<200nm) than the α_1 rods.

3.3 Morphology and structure of the Cu-enriched phase

The Cu-enriched phase that connecting α_1 phase in Fig. 2a was further investigated by using high-resolution HAADF-STEM imaging. Figure 4 (a) and (d) show two Cu-enriched rods with square and elliptical-shape cross-sections, respectively. The images were taken along the [100] zone axis of the α_2 phase. The inverse fast-Fourier-transform (FFT) images (Fig. 4(b,e)), obtained by selecting just the (0 0 1) superlattice spots from the $L2_1$ ordering in the α_2 phase only, shows that the Cu-enriched phase is located entirely within the α_2 matrix. There is an obvious difference on faceting of the Cu-enriched phase depending on its cross-sectional size.

The square-shaped Cu-enriched rods generally have smaller diameter and tend to facet on {100} planes. The corresponding FTT pattern (Fig.4 (c)) shows almost symmetric streaking (~5°) along four (110) diffraction spots of the α_2 matrix (indicated by red arrows), which implies an equal amount of tilting in those "{110}" planes in the Cu-enriched clusters from the matrix. Measurement of the angle between two "{110}" planes inside the Cu rods shows that for the first several layers from the periphery of the Cu-enriched phase, the angle between two orthogonal "{110}" planes is 90°, which is the same as the $L2_1$ structure, however, that angle of these planes undergoes a shearing to 79° at the center of the Cu-enriched phase. The (002) spots have satellite spots along the <002> direction (indicated by yellow arrows), indicative of a lattice parameter

difference between the Cu-enriched phase and matrix along the <002> direction and [100] $_{\alpha 2}$ //$[100]_{Cu}$.

The larger Cu rods (Fig. 4 (d)) have a diamond shaped cross-sections with {110} faceting. Corresponding FFT diffraction patterns show that one set of the {110} spots has no streaking, but the other set has a streaking and satellite spots which are tilted ~10° away (indicated by red arrows). This indicates that the "(1$\underline{1}$0)" plane of Cu is parallel to the (1$\underline{1}$0) plane of α_2, but the "($\underline{1}$10)" plane is tilted further away from the ($\underline{1}$10) plane of the α_2 matrix. A measurement of the angle between two "{110}" planes in Cu shows that it has an angle of 79° as well. Additionally, the {002} spots showed streaking along the <110> direction, which indicates the {002} planes of the α_2 matrix and the Cu-enriched phase are not parallel. This result suggests that the Cu-enriched phase has a body-centered tetragonal structure. When the diameter of the rods is small, they have an isotropic strain inside. With increasing diameter, the crystal will shear along a specific direction and form a blade-like structure, with one of the two possible variants (Fig. 2a). This result together with the observation along their longitudinal project indicates that the Cu-enriched phase forms an additional separation of the magnetic phase.

3.4 Morphology and movement of magnetic domains in alnico alloys.

In alnico, the magnetic domain structure is closely related to the nanometer size spinodal phase assembly. Lorentz microscopy is a unique method that provides direct observation of magnetic domains down to angstrom spatial resolution. Magnetic domain with different in-plane magnetization will deflect electron trajectory differently due to Lorentz force.[22] Domain wall is revealed as lines of light and dark contrast in Fresnel mode. Here we use Lorentz microscopy to reveal the relationship between magnetic domain structure and α_1 rods, as well as the domain wall movement process under an external magnetic field. Stripe-shape domains with widths

between 100 to 500nm, and lengths larger than 1μm were observed. Previously published reconstructed holography phase maps revealed that several α_1 rods coupled and formed 180º micromagnetic domains [23]. In Fig. 5, the objective lens (OL) in the TEM was used to apply an in-plane magnetic field on a tilted TEM sample (alpha: ±30°) to study domain wall movement *in situ*. The magnitude of the field is proportional to the OL current, while the direction of the field can be reversed by tilting the sample to the opposite direction. Considering the shape anisotropy of the α_1 rods, the TEM sample was loaded into the microscope with the magnetic field applied during annealing perpendicular to the α tilting axis of the sample holder, so that the in-plane magnetic field created by the objective lens will be parallel to the easy axis of the α_1 rods. Domain wall movement from the same area was observed and recorded in Lorentz mode, as shown in Fig 5. Large amounts of domain walls (black and white lines) were observed in the demagnetized state (Fig. 5a). With gradual increase of the applied magnetic field, initially there is no domain wall movement until the field reaches ~1.5KG, whereupon frequent domain wall movement was observed (Fig. 5b). The domain walls always sweep across one or more α_1 rods very quickly and stop at the α_1/α_2 interface, which suggests that the α_1/α_2 phase boundaries may play an important role in determining the coercivity of the alnico alloys. Finally, the sample was magnetized along the external magnetic field direction (Fig. 5c). When the magnetic field was gradually decreased to 0 along the same direction, there was no appearance of domain walls inside the grain (Fig. 5d), implying that the nano-sized rod shape of the α_1 rods were responsible for the high hysteresis loop squareness of alnico. Application of a magnetic field along opposite direction showed that domain wall movement initially started at the grain boundary region, then nucleation of small domains was observed to appear close to the grain boundary (Fig. 5 e). When

the field reached ~1.4KG, a large number of domain walls were observed inside the grain (Fig. 5f). Further increase of the magnetic field magnetized the sample along the opposite direction.

3.5 Discussion

The above observed microstructures well explain the discrepancy between the theoretical prediction and the experimental maximum of magnetic properties in alnico. First, the directionally cast grains are not all well aligned with <001> crystallographic direction. Previous study has shown that the SD morphology was closely related to the relationship between the <100> and the external field during magnetic field annealing. The α_1 rods tend to elongate to the <100> with the largest projected external field.[23] Misalignment of grains to the <100>, particularly from the edge of the cast block, will reduce the squareness of hysteresis loop and $(BH)_{max}$ of the magnets. Second, the Fe-rich phase at the grain boundaries showed magnetization reversal with lower external field, implying that grain boundaries may act as a nucleation site for domain reversal and are not good for enhancing the H_{ci} of alnico, which is consistent with literature reports.[24] Thirdly, porosity in the alloy is likely inhibiting the magnetic performance, reducing the phase fraction of the magnetic alloy and reducing grain alignment. Additionally, the presence of TiS_2 in the microstructure is a new discovery, pointing to the underlying mechanism by which S additions promote columnar grains in higher Ti containing alloys. [25] The S ties up some Ti in the microstructure, lowering the Ti available for grain refinement.

The difference between theoretically achievable coercivity and experimentally measured values is explained by the diameter of the α_1 phase being much larger than the optimal diameter of the magnetic nano-rods assuming a coherent rotation ($2R_{coh}$ = 12.8 nm) mechanism used in the micromagnetic modeling.[9, 26] *In situ* magnetization in TEM showed that the α_1 rods connected by branches tend reverse at the same external magnetic field, this confirms the

modeling that branching segments act as short circuits to domain rotation and allow for a cascading domain reversal at lower applied fields.[26] The EDS mapping clearly shows that the Cu-enriched rods extending along the rod boundaries and in some cases providing additional separation (Fig. 3). Controlling the size and distribution of the Cu-enriched phase may indeed be another route to increasing coercivity by limiting the continuous branching.

Further property improvement of alnico 9 can be achieved by optimizing various aspects of the alloy's microstructure. Primarily by increasing grain orientation uniformity along the magnetization direction, reducing detrimental grain boundary phase volume fraction, and minimizing branching of the α_1 rods, as well as their diameter. This can be achieved through better processing control such as improved directional solidification [7], modifying the chemistry to better control the phase fraction of the α_1 phase relative to the matrix and by controlling the post solidification processing to reduce the diameter of the spinodal. Better understanding of the critical microstructural features are also helping to guide reducing Co content without sacrificing magnetic properties. [20]

4. Conclusions

A comprehensive structural characterization of alnico 9 was performed down to the atomic level. Porosity, TiS_2 precipitates, and some grain misorientation were observed at different regions of the directionally solidified casting, which also brings a difference in magnetic properties. Inside each grain, a "mosaic structure" is formed by {110} or {100} planar faceted α_1 rods (~35nm) embedded in an α_2 matrix. There is also a Cu-enriched phase residing at the corners of two <110> facets of the α_1 phase. The nanoscale isolated α_1 rods are the microstructural feature that gives rise to the high coercivity of alnico. The grain boundary phases reverse magnetization direction at lower applied magnetic field compared with the SD region

inside the grain. Obseravtions here confirm recent micromagnetic modeling that both the size and the branching of the α_1 rods are crucial to improving coercivity. Further enhancement of alnico magnets performance can be approached by increasing grain orientation uniformity through improved directional solidification and decreasing α_1 rod diameters, branching, and grain boundary phases through chemical modifications and improved post solidification heat treatment. With the increasing strategic importance of Co, these guidelines are enabling reduced Co.

Acknowledgement

Research was supported by U.S. DOE, Office of Energy Efficiency and Renewable Energy (EERE), under its Vehicle Technologies Program, through the Ames Laboratory, Iowa State University under contract DE-AC02-07CH11358. Part of the TEM work was conducted at ORNL's Center for Nanophase Materials Sciences (CNMS), which is a DOE Office of Science User Facility. Sandia National Laboratories is a multi-program laboratory managed and operated by National Technology and Engineering Solutions of Sandia, LLC., a wholly owned subsidiary of Honeywell International, Inc., for the U.S. Department of Energy's National Nuclear Security Administration under contract DE-NA0003525. The authors would like to thank FEI Company for helping longitudinal TEM EDS mapping.

References:

[1] R.W. McCallum, L.H. Lewis, R. Skomski, M.J. Kramer, I.E. Anderson, Practical Aspects of Modern and Future Permanent Magnets, Annu Rev Mater Res, 44 (2014) 451-477.
[2] R. Skomski, P. Manchanda, P. Kumar, B. Balamurugan, A. Kashyap, D.J. Sellmyer, Predicting the Future of Permanent-Magnet Materials, Ieee T Magn, 49 (2013) 3215-3220.
[3] M.J. Kramer, R.W. McCallum, I.A. Anderson, S. Constantinides, Prospects for Non-Rare Earth Permanent Magnets for Traction Motors and Generators, Jom-Us, 64 (2012) 752-763.
[4] I.E. Anderson, A.G. Kassen, E.M.H. White, L. Zhou, W. Tang, A. Palasyuk, K.W. Dennis, R.W. McCallum, M.J. Kramer, Novel pre-alloyed powder processing of modified alnico 8: Correlation of microstructure and magnetic properties, J Appl Phys, 117 (2015).
[5] K. Hono, H. Sepehri-Amin, Strategy for high-coercivity Nd-Fe-B magnets, Scripta Mater, 67 (2012) 530-535.
[6] S. Sugimoto, Current status and recent topics of rare-earth permanent magnets, J Phys D Appl Phys, 44 (2011).
[7] M. Zou, F. Johnson, W.M. Zhang, Q. Zhao, S.F. Rutkowski, L. Zhou, M.J. Kramer, Processing of alnico permanent magnets by advanced directional solidification methods, J Magn Magn Mater, 420 (2016) 152-157.
[8] R. Skomski, Y. Liu, J.E. Shield, G.C. Hadjipanayis, D.J. Sellmyer, Permanent magnetism of dense-packed nanostructures, J Appl Phys, 107 (2010).
[9] H. Zeng, R. Skomski, L. Menon, Y. Liu, S. Bandyopadhyay, D.J. Sellmyer, Structure and magnetic properties of ferromagnetic nanowires in self-assembled arrays, Phys Rev B, 65 (2002).
[10] M.K.M. L. Zhou, H. Dillon, A. Palasyuk, S. Constantinides, R.W. McCallum, I. E. Anderson, and M. J. Kramer, Role of the Applied Magnetic Field on the Microstructural

Evolution in Alnico 8 Alloys, Metallurgical and Materials Transactions E, 1E (2014) 27.
[11] Y. Iwama, Magnetic Properties of Alnico-Type Magnet Alloys at Elevated Temperatures, T Jpn I Met, 8 (1967) 18-&.
[12] Y. Iwama, On Magnetic Powder Patterns of High-Coercivity Alnico 5 Magnet Alloys, T Jpn I Met, 9 (1968) 273-&.
[13] Y. Iwama, M. Inagaki, T. Miyamoto, Effects of Titanium in Alnico 8-Type Magnet Alloys, T Jpn I Met, 11 (1970) 268-&.
[14] Y. Iwama, M. Takeuchi, Spinodal Decomposition in Alnico-8 Magnet Alloy, T Jpn I Met, 15 (1974) 371-377.
[15] R.A. McCurrie, Ferromagnetic materials 3, North-Lolland Publishing Company, UK, DOI (1982).
[16] W. Schafer, E. Jansen, W. Kockelmann, A. Alker, A. Kirfel, D. Seitz, M. Gronefeld, Variations of microstructure and texture of permanent magnetic Alnico alloys, Physica B, 276 (2000) 866-867.
[17] V. Sergeyev, T. Bulgina, Magnetic Properties of Alnico Alloy Phases and Temperature Instability of Permanent Magnets, J Appl Phys, 40 (1969) 1307-&.
[18] V. Sergeyev, T.Y. Bulygina, Magnetic Properties of Alnico-5 and Alnico-8 Phases at Sequential Stages of Heat Treatment in a Field, Ieee T Magn, Mag6 (1970) 194-&.
[19] V. Sergeyev, Larichki.Ry, Relation of Magnetic Properties to Structural Perfection in Alnico Single Crystals, Ieee T Magn, Mag6 (1970) 239-&.
[20] R.W.M. Andriy Palasyuk, Iver E. Anderson, Matthew Kramer, Lin Zhou, Wei Tang., US patent application, DOI (2017).
[21] P. Lu, L. Zhou, M.J. Kramer, D.J. Smith, Atomic-scale Chemical Imaging and Quantification of Metallic Alloy Structures by Energy-Dispersive X-ray Spectroscopy, Scientific Reports, 4 (2014).

[22] D.B.W.a.C.B. Carter, Transmission Electron Micrsocopy, Plenum Press, USA, DOI (1996).
[23] L. Zhou, M.K. Miller, P. Lu, L.Q. Ke, R. Skomski, H. Dillon, Q. Xing, A. Palasyuk, M.R. McCartney, D.J. Smith, S. Constantinides, R.W. McCallum, I.E. Anderson, V. Antropov, M.J. Kramer, Architecture and magnetism of alnico, Acta Mater, 74 (2014) 224-233.
[24] C.A. Julien, F.G. Jones, Alpha-Sub-Gamma Phase in Alnico 8 Alloys, J Appl Phys, 36 (1965) 1173-&.
[25] N. Makino, Y. Kimura, Techniques to Achieve Texture in Permanent Magnet Alloy Systems, J Appl Phys, 36 (1965) 1185-+.
[26] L.Q. Ke, R. Skomski, T.D. Hoffmann, L. Zhou, W. Tang, D.D. Johnson, M.J. Kramer, I.E. Anderson, C.Z. Wang, Simulation of alnico coercivity, Appl Phys Lett, 111 (2017).

Table 1. Magnetic properties of different 1 inch tall sections of the alnico 9 casting.

Magnet ID	Br (G)	Hci (Oe)	BHmax (MGOe)	Squareness (Hk/Hci)
Top	10,780	1,414	8.35	0.66
Middle	11,210	1,374	10.56	0.86
Bottom	10,830	1,416	9.20	0.73
Average	10,940	1,401	9.37	0.75

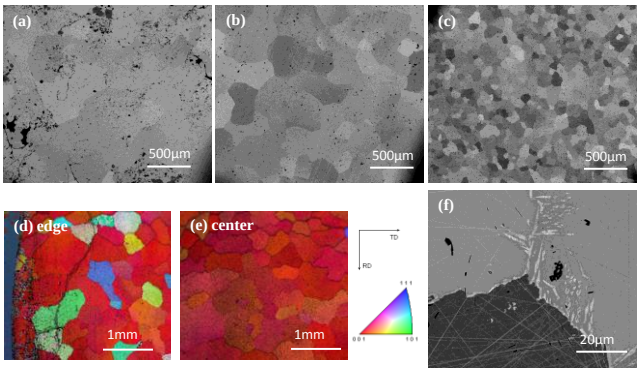

Fig. 1 Zhou et al

SEM and EBSD images showing TiS_2 precipitates, grain size and orientation (according to included inverse pole figure). A) top of casting, B) middle of casting, C) bottom of casting. D) and E) EBSD of middle sample in different locations of the casting. F) higher magnification image of the bottom of the casting.

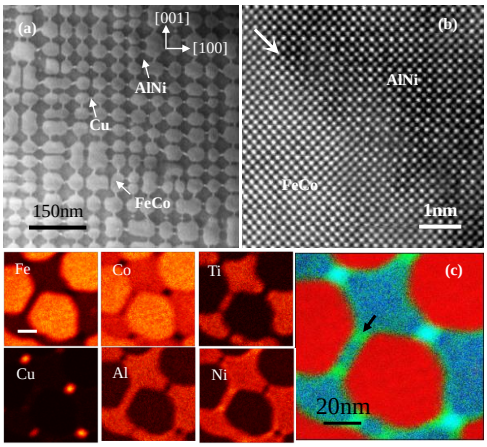

Fig. 2 Zhou et al

(a) HAADF STEM image of alnico 9(transverse) showing "mosaic" structure. (b) High resolution HAADF STEM image taken under [100] zone axis showing coherent α_1/α_2-rich interface. (c) Elemental mapping and color composite image (red: FeCo; green: Ni; blue: AlNi) of the "mosaic" structure. Ni-enriched clusters is indicated by black arrow. The scale bar in EDS maps is 20nm.

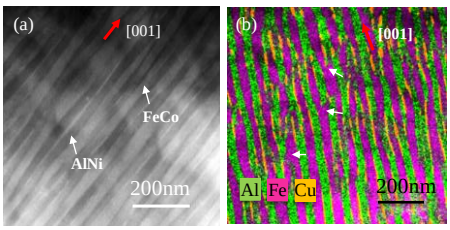

Fig. 3 Zhou et al

(a) HAADF STEM image of alnico 9 (L). (b) color composite image using Al (green), Fe (magenta) and Cu (orange) signal. The branches of α_1 rods are indicated by white arrows.

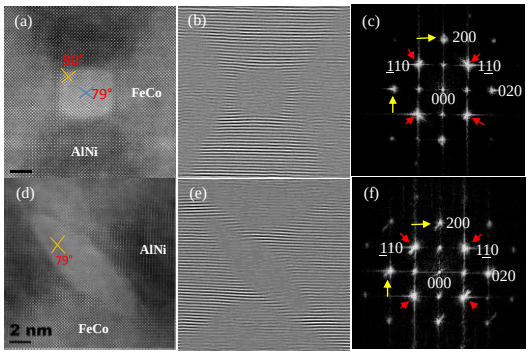

Fig. 4 Zhou et al

(a) HR-STEM images of a square-shaped Cu-enriched phase with corresponding FFT. The image was taken under [001] zone axis. (c) and filtered inverse FFT using only the (001) superlattice spots (b). (d) HR-STEM images of a elliptical-shaped Cu-enriched phase with corresponding FFT (f) and filtered inverse FFT using only the (001) superlattice spots (e).

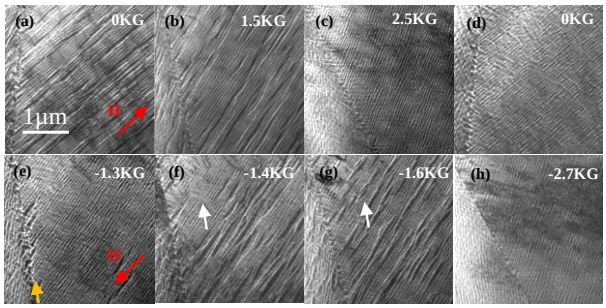

Fig. 5 Zhou et al

Lorentz images of alnico 9(longitudinal) with different applied external magnetic field within TEM. Grain boundary region reverse at the lower applied field (indicated by yellow arrow in d) and branched α_1 rods flip in concert (indicated by white arrows in e and f).

- The nanoscale isolated α_1 (FeCo-rich) and Cu-enriched rods are the microstructural feature that gives rise to the high coercivity of alnico.
- *In situ* Lorentz microscopy revealed that the grain boundary phases reverse magnetization direction at lower applied magnetic field compared with the SD region inside the grain.
- Porosity, TiS_2 precipitates, and some grain misorientation were observed at different regions of the directionally solidified casting, which also brings a difference in magnetic properties.